Supplementary Information

A self-powered hydrogel electronic skin with decoupled multimodal sensing for closed-loop human-machine interactions

Chenhui Bai [1,2,†], Xinyu Dong [2,†], Quyang Liu [2], Ming Zhao [1], Kun Yang [1], Yu Niu [1], Hulin Zhang [1]*, Wei Zhai [2]*

[1]College of Integrated Circuits, Taiyuan University of Technology, Taiyuan, 030024 China

[2]Department of Mechanical Engineering, National University of Singapore, 9 Engineering Drive 1, Singapore, 117575 Singapore

[†]These authors contributed equally to this work.
*Correspondence: zhanghulin@tyut.edu.cn(H.Z.); mpezwei@nus.edu.sg(W.Z.)

Table of Contents

Supplementary Note

Supplementary Note 1: Molecular dynamics simulation methods

Classical molecular dynamics (MD) simulations were performed to investigate the microscopic structures of Fe^{3+} and Fe^{2+} in water and PVA solutions at the atomic level. The components and their quantities of the two simulated systems are listed in Supplementary Table 5 and 6. Initial configurations of two solvent systems were constructed using PACKMOL software[1], with all molecules randomly inserted in a cubic simulation box. The SPC/E model, which had been validated for accurate water simulation, was used as the force field of H_2O. The OPLS-AA force field[2] was employed to describe PVA, Fe^{2+}, Fe^{3+}, and Cl^- molecules. The molecular force field consisted of both bonded and nonbonded interactions. The nonbonded interactions included van deer Waals (vdW) and electrostatic interactions, as described by the following equations, respectively:

$$E_{LJ}(r_{ij}) = 4\varepsilon_{ij}\left(\left(\frac{\varepsilon_{ij}}{r_{ij}}\right)^{12} - \left(\frac{\varepsilon_{ij}}{r_{ij}}\right)^{6}\right) \quad (1)$$

$$E_c(r_{ij}) = \frac{q_i q_j}{4\pi\varepsilon_o\varepsilon_r r_{ij}} \quad (2)$$

For different atom types, the Lorentz-Berthelot mixing rules were applied for vdW interactions, as given in the equation below:

$$\sigma_{ij} = \frac{1}{2}(\sigma_{ii} + \sigma_{jj}); \varepsilon_{ij} = (\varepsilon_{ii} * \varepsilon_{jj})^{\frac{1}{2}} \quad (3)$$

The cutoff distance for vdW and electronic interactions was set to 1.2 nm, and the particle mesh Ewald (PME) method was employed to calculate long-range electrostatic interactions.

For each simulation, energy minimization was first performed to relax the simulation box. This was followed by an isothermal–isobaric (NPT) ensemble simulation with a 1.0 fs time step, where the temperature was maintained at 300 K and the pressure at 1.0 atm using the Nosé–Hoover thermostat and Parrinello–Rahman barostat, respectively.

The NPT optimization was run for 400 ps, which was sufficient to obtain a stable box size. Subsequently, a canonical (NVT) ensemble simulation was conducted for 300 ps with a 1.0 fs time step to further optimize the system. The optimized simulation boxes are shown in Figure 2. In all MD simulation, atomic motion was described by classical Newton's equations of motion, solved by the velocity-Verlet algorithm. All simulations were performed using the LAMMPS package[5].

Supplementary Note 2: Finite element analysis methods

Finite element analysis (FEA) of coupled poroelastic solvent flow, ion transport, and electrostatic calculations were conducted using COMSOL. A prismatic hydrogel with a rectangular base was modeled (Figure 3i). A stainless-steel plate was placed on top to compress the hydrogel in the z-direction, while the bottom surface was fixed in all directions (x, y, and z displacements were constrained to zero). All other surfaces were free to deform. The simulation geometry is shown in Supplementary Figure 22.

When the liquid phase was set to water, an elastic polymer matrix was modeled in the poroelasticity module as a solvent-containing medium, where fluid convection occurs upon applied pressure. Flow continues until the applied pressure is balanced by the elastic restoring force generated by expansion of the polymer at the base. Darcy's law was used to simulate liquid flow within the polymer matrix in a transient analysis, as described by the equations below:

$$\nabla\sigma_e \cdot \Omega = \mu_c \tag{4}$$

$$V_i = \frac{-\kappa}{\eta}\nabla P \tag{5}$$

where σ_e is the total elastic stress of the polymer (N m^{-2}), Ω is the molar volume of a solvent molecule (mol m^{-3}), μ_c is the chemical potential of electrolyte molecules inside the gel (J mol^{-1}), V_i is the Darcy's velocity, κ is the permeability of the gel (m^2), η is the fluid viscosity (Pa·s), and ∇P is the pressure gradient within a gel (Pa m^{-1}). The polymer matrix and fluid property parameters used are summarized in Supplementary Table 5.

The output voltage depends on the balance between the rate of charge diffusion and the amount of charge, as solvent flow carries charge and creates a voltage gradient. By substituting V_i into the transport eigen equations yields the convection, diffusion, and migration relation:

$$N_i = v_i c_i - D_i \nabla c_i - z_i c_i \mu_i \nabla V \tag{6}$$

where N_i is the molar flux of species i in the solvent (mol $m^{-2}s^{-1}$), v_i is the convection velocity (m s^{-1}) of a given electrolyte species, c_i is the concentration (M), D_i is the diffusion coefficient (m^2 s^{-1}), z_i is the valence charge, and μ_i is the electrophoretic mobility.

When compressive strain is applied to the hydrogel, the concentrations of both anions and cations increase, where convection-driven concentration differences become the dominant factor. The advection equation defines the molar flux of ions due to the concentration gradient:

$$J = v_{\mathrm{i}} c_{\mathrm{i}} \tag{7}$$

The total current density can be expressed as:

$$J = \sum n_{\mathrm{i}} z_{\mathrm{i}}\, e v_{\mathrm{i}} \tag{8}$$

where n_i is the ion concentration. Therefore, the compression-induced current density can be regarded as a net ionic current:

$$J = ev(n_+ Z_+ - n_- Z_-) \tag{9}$$

where $n_{+/-}$ are the concentrations of cations ($Fe^{2+/3+}$) and anions (Cl^-), respectively, and $Z_{+/-}$ are their corresponding charges.

A schematic side view of the prism structure is shown in Supplementary Figure 21, where *p* is the side length at the bottom of the prism, *q* is the side length at the top, *h* is the prism height, *a* is a variable ranging from 0 to *b*, and *b* represents the proportion at which the two forces reach equilibrium. The area of the surface of the top deformed region is

$$S = \left(q + (p - q)\frac{a}{h}\right)^2 \tag{10}$$

Given *E* as the effective Young's modulus of the prismatic hydrogel, the elastic force generated on the deformed region can be described as:

$$f = \int_0^b df = \int_0^b E \cdot \frac{a}{h} dS = \frac{E(p-q)b^2}{h^2}\left(q + \frac{2(p-q)b}{3h}\right) \tag{11}$$

The total elastic force is:

$$F_e = N \cdot f \tag{12}$$

where N is the number of prisms.

However, considering mechanical loss, the applied force can be expressed as $k \cdot F$, where k is the mechanical transfer efficiency and F_e is the external elastic force. At equilibrium,

$$F = k \cdot F_e = k \cdot N \cdot E \cdot \frac{(p-q)b^2}{h^2}\left(q + \frac{2(p-q)b}{3h}\right) \tag{13}$$

The ion velocity v is determined by Darcy's law:

$$v = \frac{\kappa}{\eta}\nabla P = \frac{\kappa}{\eta} \cdot \frac{F}{hS} \tag{14}$$

where κ is the permeability, η is the viscosity, and S is the cross-sectional area.

The output current I is defined as the integral of the current density J over the cross-sectional area S as:

$$\begin{aligned} I &= \int J dS = \frac{e\kappa(n_+ Z_+ - n_- Z_-)}{\eta h} \cdot F \\ &= \frac{e\kappa(n_+ Z_+ - n_- Z_-)}{\eta h} \cdot k \cdot N \cdot E \cdot \frac{(p-q)b^2}{h^2}\left(q + \frac{2(p-q)b}{3h}\right) \end{aligned} \tag{15}$$

According to this formula, the output current is linearly proportional to the applied pressure. In addition, the sensitivity depends on the Young's modulus of the hyperplastic PVA hydrogel.

Supplementary Figure

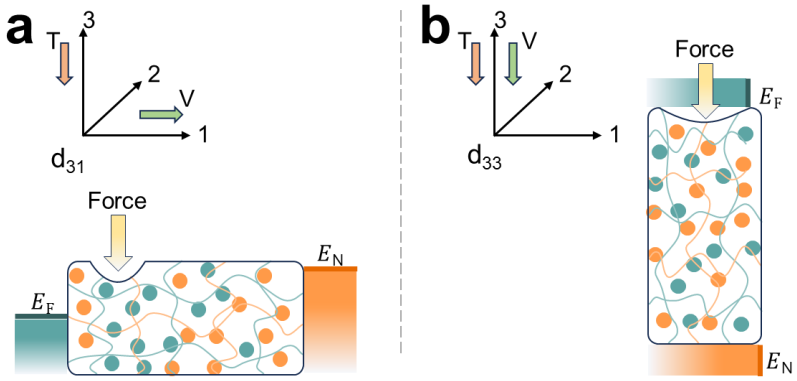

Supplementary Figure 1. The (a) d_{31} and (b) d_{33} modes of the piezoionic effect.

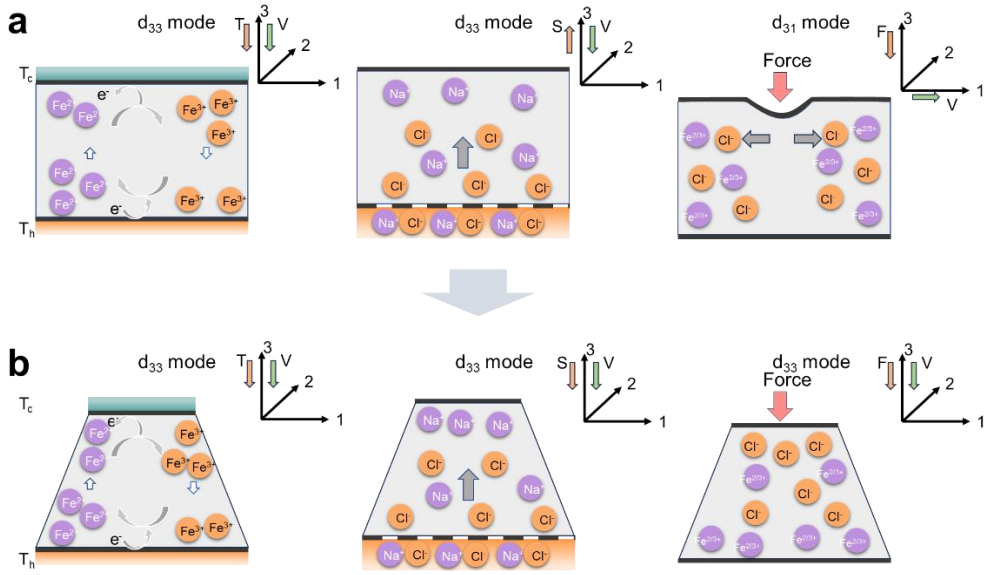

Supplementary Figure 2. Schematic illustrations of the thermogalvanic, diffusion, and piezoionic effects showing a transition from a mixed d_{31} and d_{33} configuration in (a) to a synergized d_{33} mode enabled by the prismatic architecture in (b).

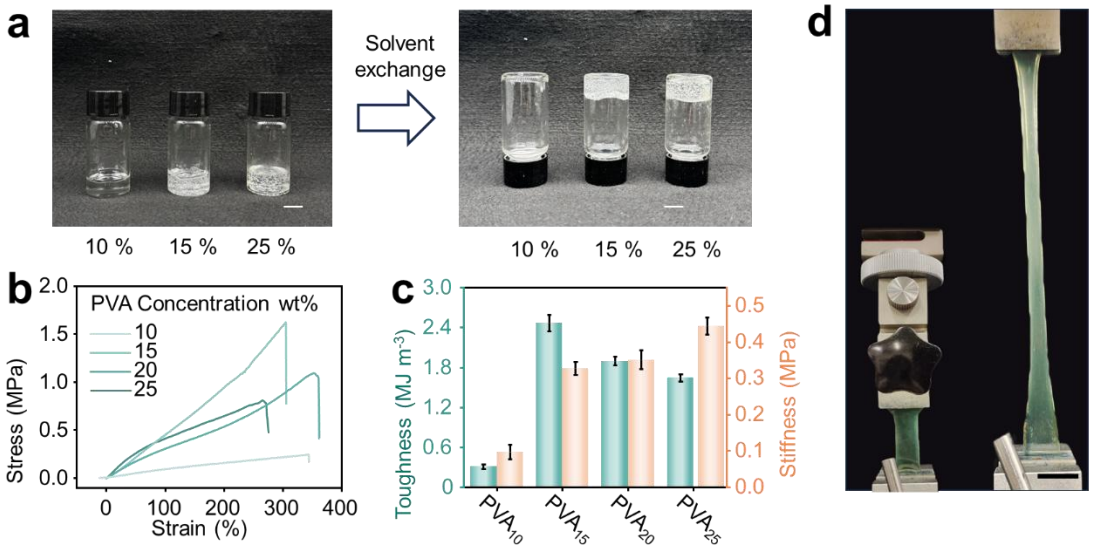

Supplementary Figure 3. (a) Photographs showing the dissolution states of PVA in DMSO at different concentrations (10, 15, and 25 wt.%). At concentrations below 10 wt.%, no aggregated network is formed (scale bar: 1 cm). (b) Stress-strain curves of hydrogels prepared with different PVA contents. (c) Toughness and stiffness at different PVA contents. (d) Photographs of tensile tests on PVA gels (scale bar: 5 mm).

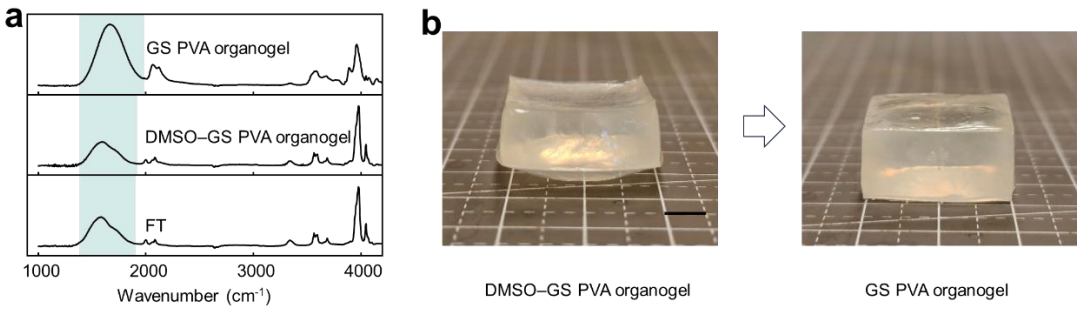

Supplementary Figure 4. (a) Fourier transform infrared spectra of the FT PVA Organogels, DMSO-GS PVA Organogels and GS Organogels[3]. (b) Comparison photos of PVA Organogels after single and double glycerol displacement.

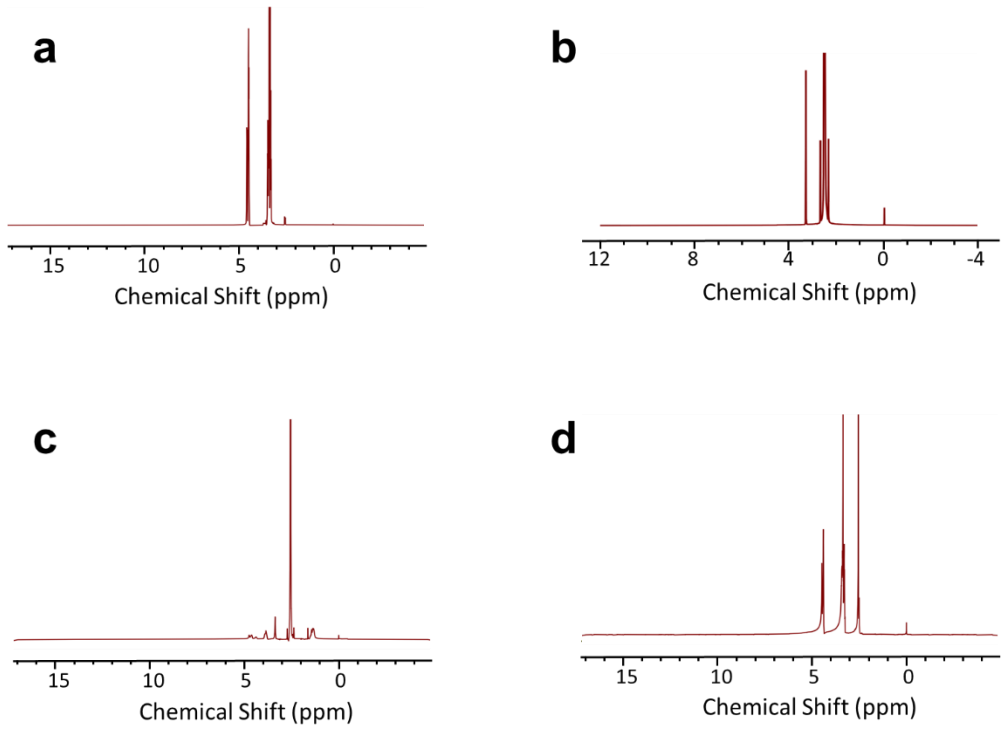

Supplementary Figure 5. ^{1}H-NMR spectra of (a) DMSO, (b) glycerol, (c) FT hydrogel, and (d) GS organogels in DMSO-d6 at 295 K.

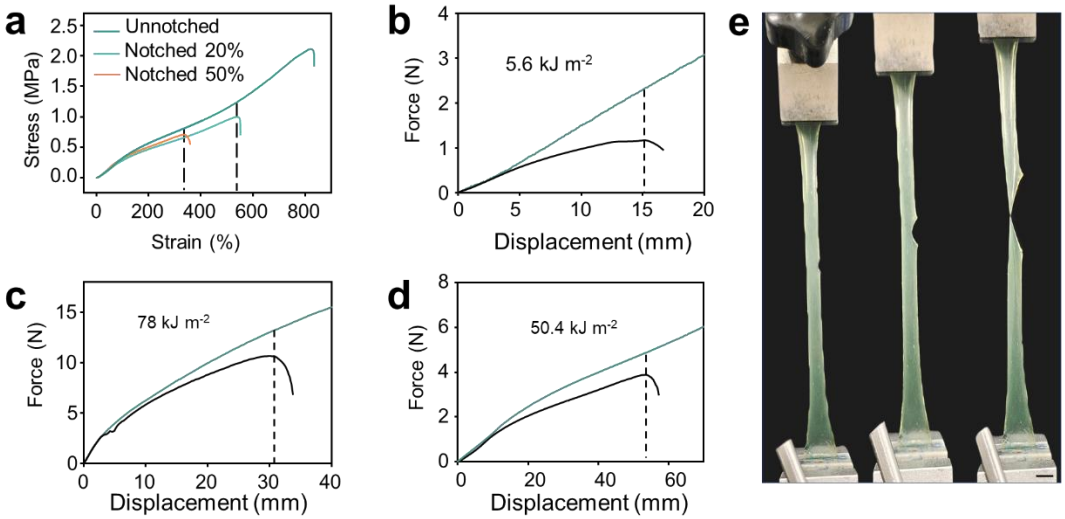

Supplementary Figure 6. (a) Fracture energy of as-prepared hydrogels. (b-d) Force-displacement curves of unnotched and notched samples of (b) FT hydrogel, (c) GS organogels, and (d) IS hydrogel. (e) Photographs of fracture tests of PVA gels (scale bar: 5 mm)[4].

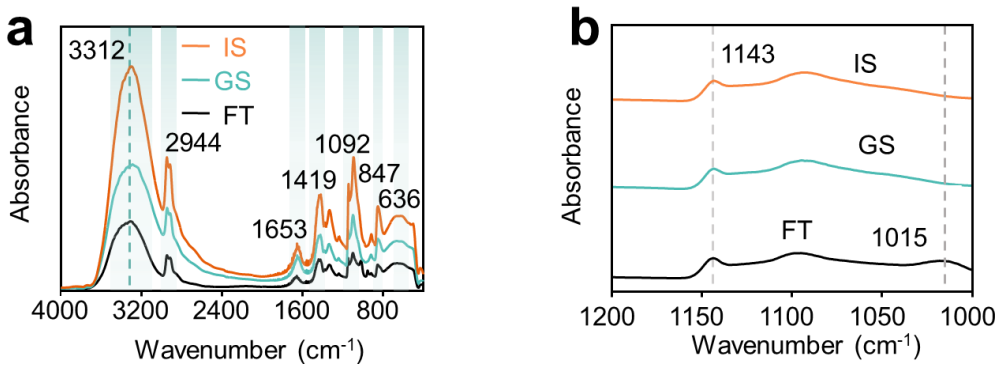

Supplementary Figure 7. Fourier-transform infrared (FTIR) spectra of PVA gels (a) at full range of 400-4000 cm^{-1} and (b) at range of 1000-1200 cm^{-1}.

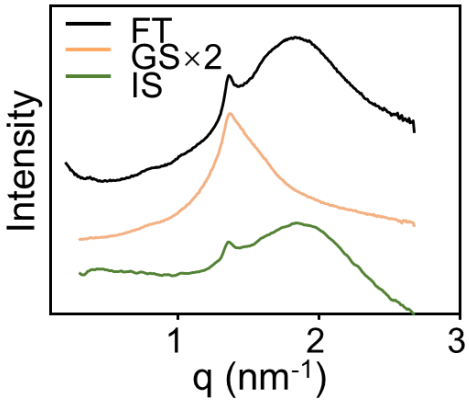

Supplementary Figure 8. 1D small-angle X-ray scattering (SAXS) profiles of FT, GS, and IS.

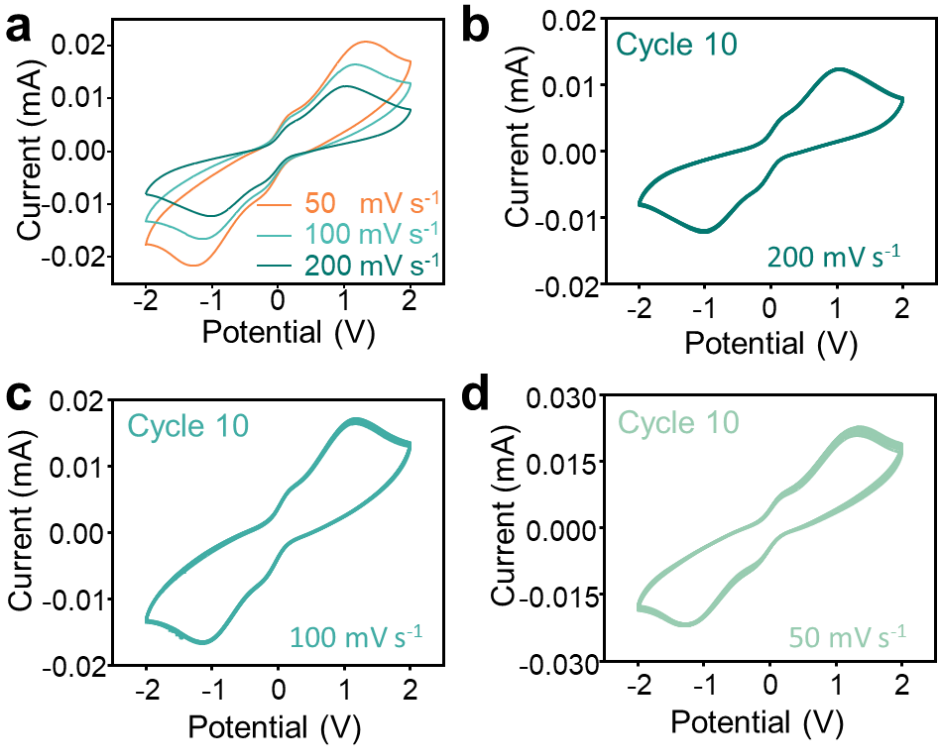

Supplementary Figure 9. Cyclic voltammetry (CV) profiles at various scan rates (T=300 K), including (b) 200mV s^{-1}, (c) 100mV s^{-1}, and (d) 50mV s^{-1}.

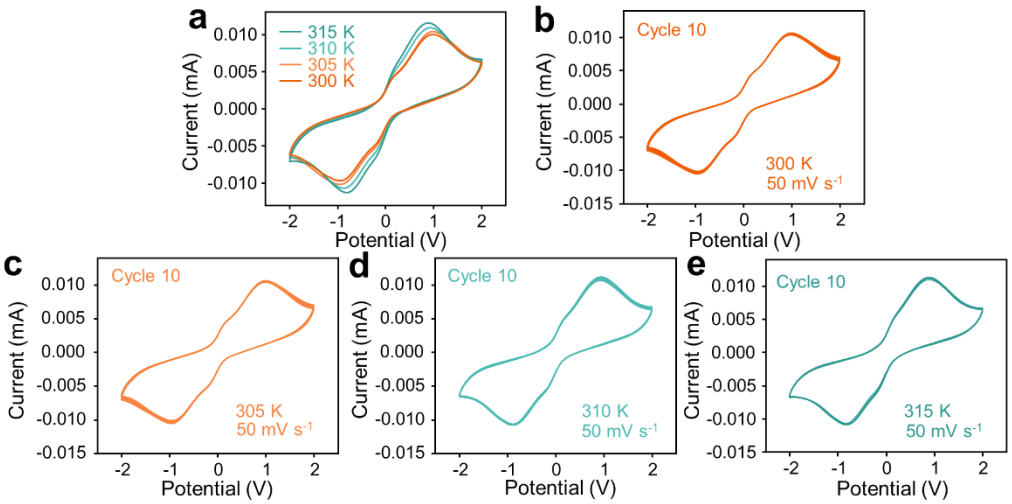

Supplementary Figure 10. (a) CV profiles at different temperatures (scan rate: 50mV s^{-1}), including (b) 300 K, (c) 305 K, (d) 310 K, and (e) 315 K.

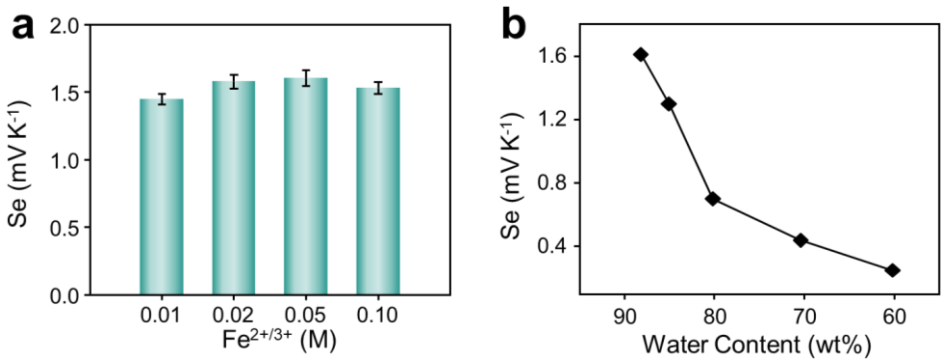

Supplementary Figure 11. (a) The Seebeck coefficient at increasing $Fe^{2+/3+}$ concentrations. (b) Seebeck coefficient varying with moisture content.

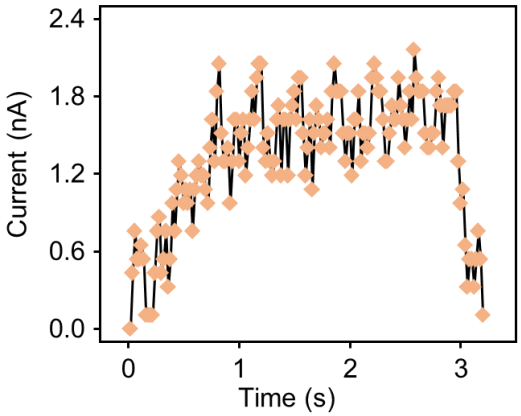

Supplementary Figure 12. Temperature detection limit. An infrared laser module was used to irradiate a section of the PVA gel to produce a temperature difference of 0.1°C.

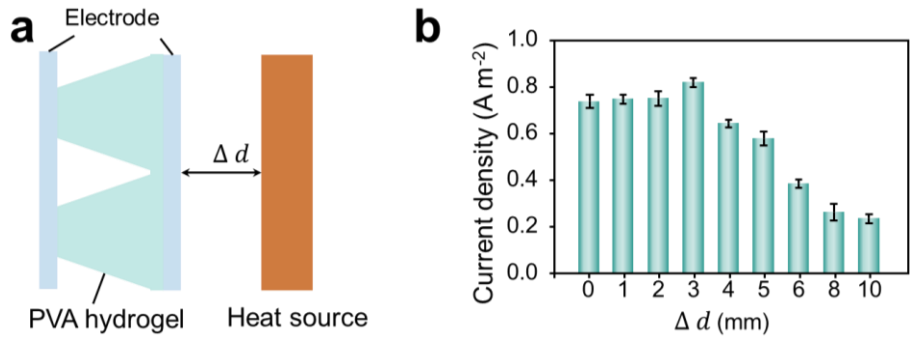

Supplementary Figure 13. Non-contact Temperature Sensing Test. (a) Current density changes as the distance between the hydrogel e-skin and the heat source decreases from 10 mm to full contact (0 mm). d is the distance from the heat source to the hot end electrode of the gel. (b) The current magnitude depends on the temperature difference between the hot and cold ends. At smaller distances, heat radiation raises the cold-end temperature, reducing the temperature difference and lowering the output current.

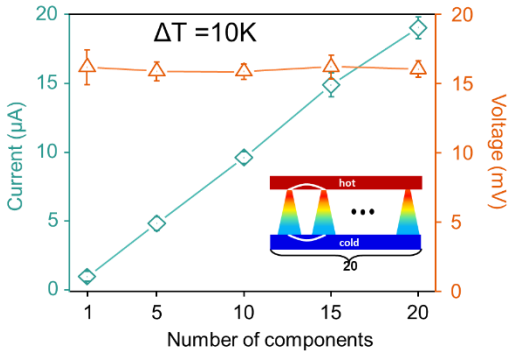

Supplementary Figure 14. Output current and voltage with 20 parallel connected units at a 10-K temperature difference. The inset shows a schematic of the integrated device.

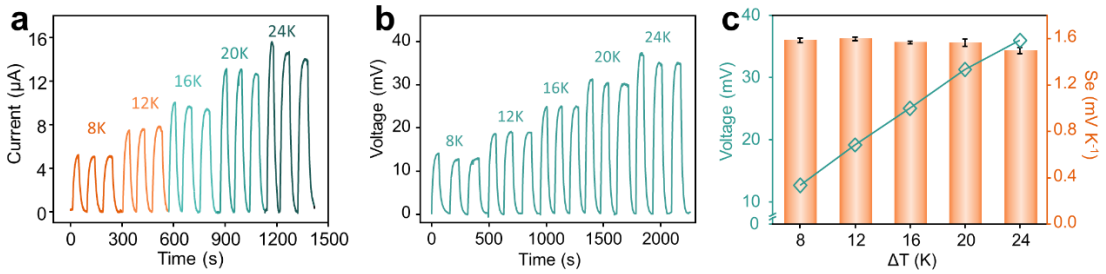

Supplementary Figure 15. Variations in (a) current, (b) voltage, and (c) calculated Se of the thermoelectric gel under different temperature differences.

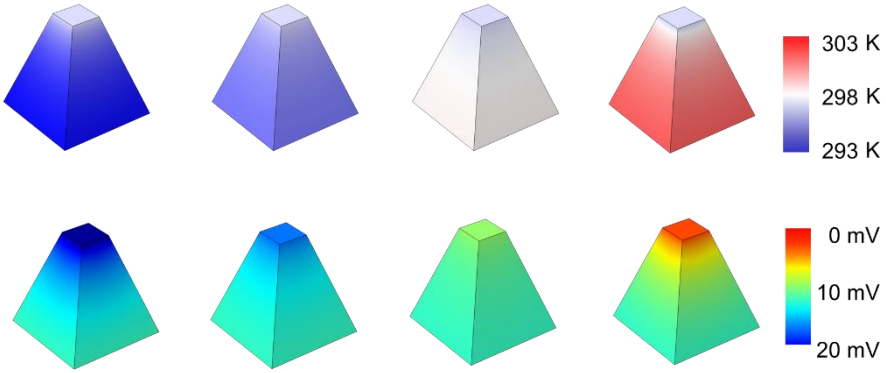

Supplementary Figure 16. Voltage variations under different temperature conditions simulated by COMSOL.

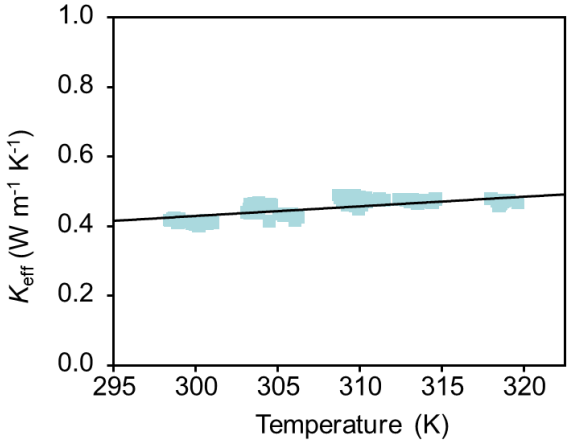

Supplementary Figure 17. Thermal conductivity of the hydrogel e-skin measured using the hot-wire method.

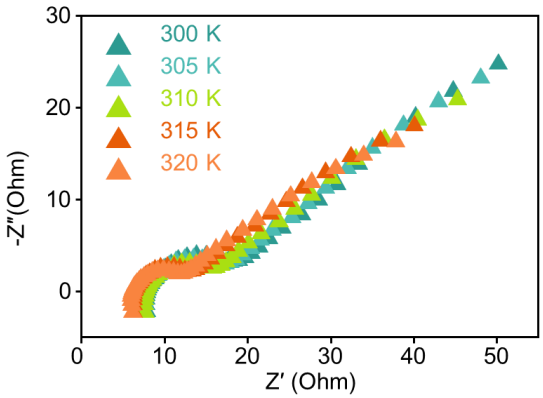

Supplementary Figure 18. Electrochemical impedance spectra (EIS) of the hydrogel e-skin under different temperatures.

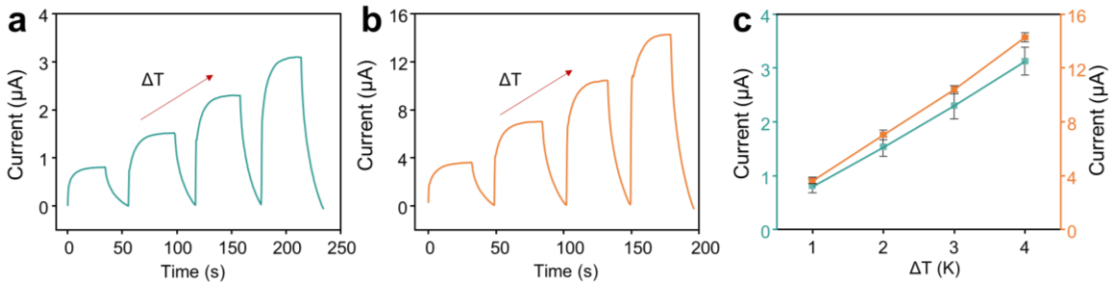

Supplementary Figure 19. Thermoelectric current comparison between prismatic (a) and cubic (b) structures. (c) Thermoelectric current against temperature difference in prismatic and cubic structures. The cold-end temperature is fixed at 30 °C.

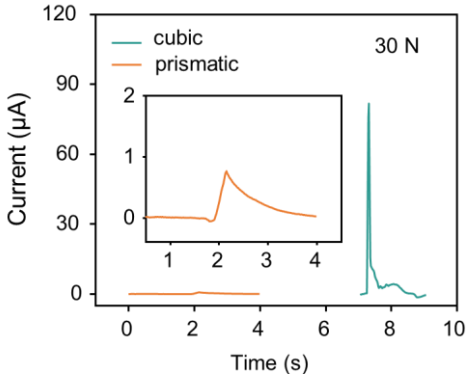

Supplementary Figure 20. For hydrogel structures with cubic and prismatic shapes having identical cross-sectional areas, the time-dependent relationship of the piezoionic current under identical load of 30N.

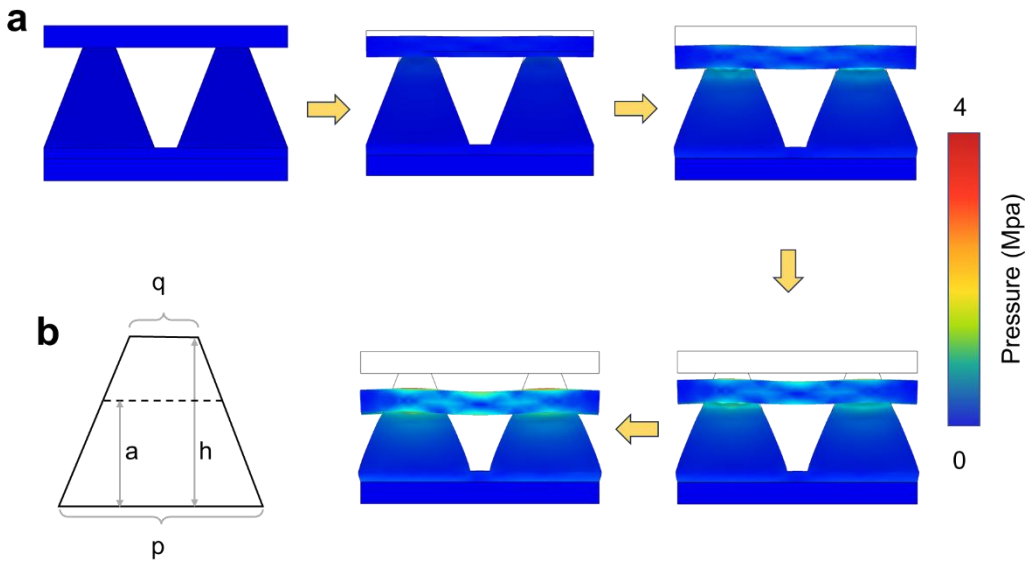

Supplementary Figure 21. (a) FEA simulation of stress distribution in the prismatic hydrogel e-skin under gradually increased pressure. (b) The schematic side view of the prism structure.

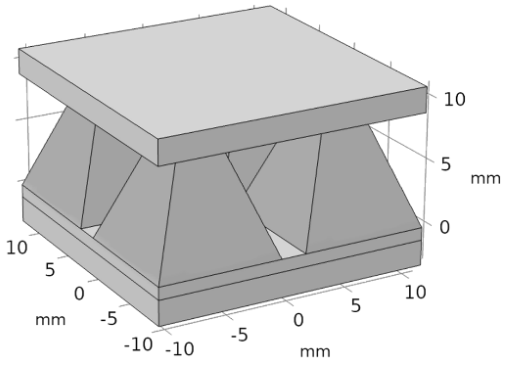

Supplementary Figure 22. Schematic of the geometry used for compression tests. The gel measures 2 cm × 2 cm × 1 cm, with a 2 cm × 2 cm rigid boundary on the top surface for applying displacement-controlled compression.

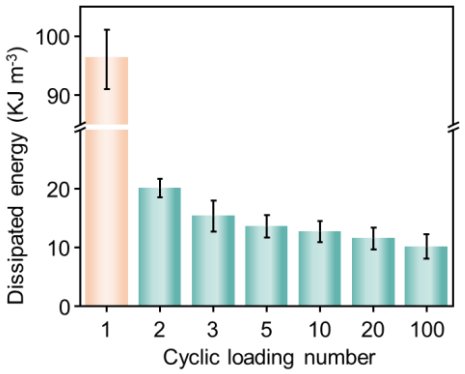

Supplementary Figure 23. Mechanical energy dissipation of the hydrogel e-skin in 100 tensile cycles.

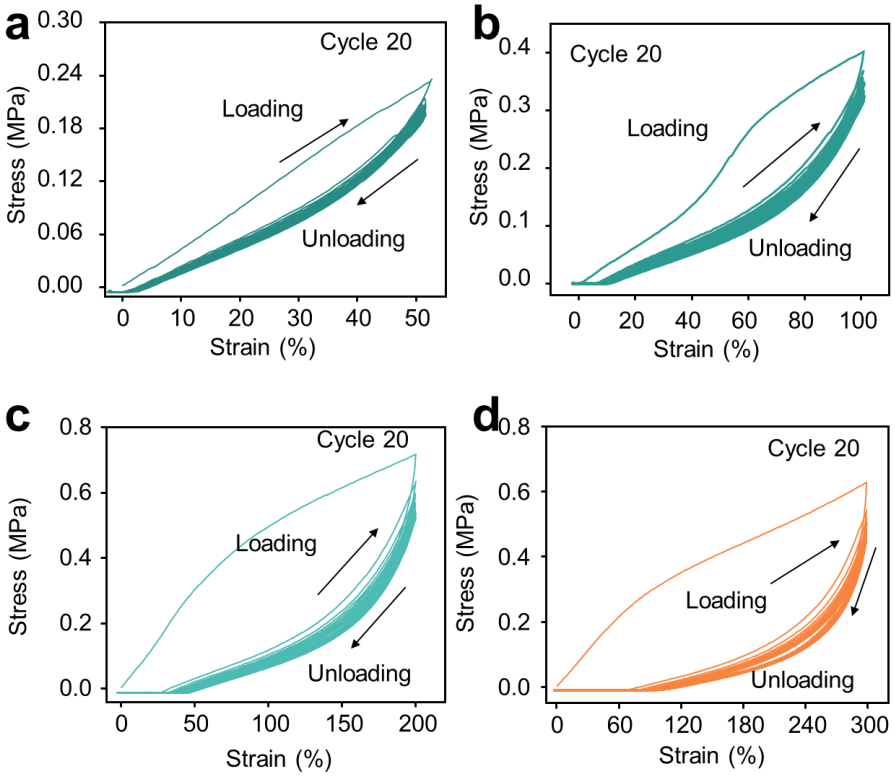

Supplementary Figure 24. Cyclic tensile stress-strain curves at increasing strain levels, including (a) 50 %, (b) 100 %, (c) 200 %, and (d) 300 %.

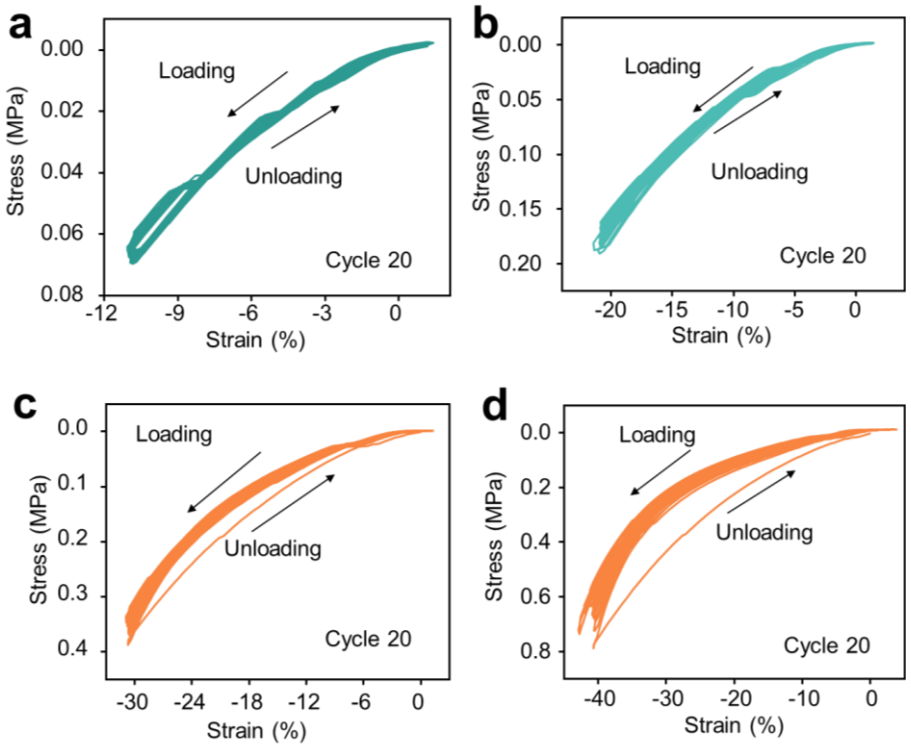

Supplementary Figure 25. Cyclic compressive stress-strain curves at increasing strain levels, including (a) 10 %, (b) 20 %, (c) 30 %, and (d) 40 %.

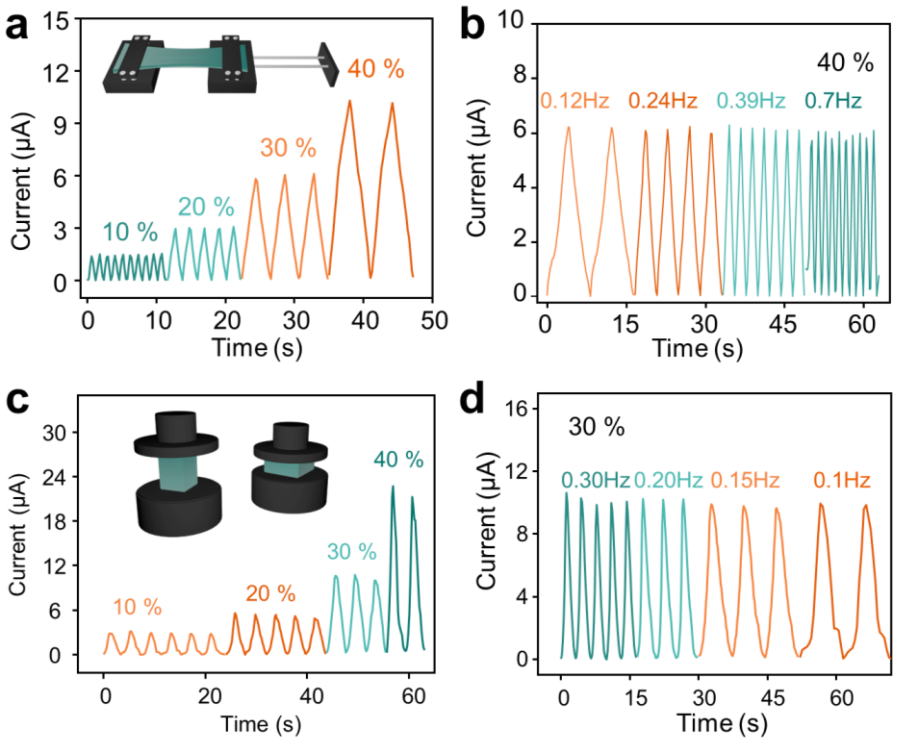

Supplementary Figure 26. Strain sensing capability of the hydrogel e-skin. (a) Current responses under tensile strains of 10%, 20%, 30%, and 40%. (b) Current responses during cyclic stretching (40% strain) at frequencies from 0.12 Hz to 0.7 Hz. (c) Current responses under compressive strains of 10%, 20%, 30%, and 40%. (d) Current responses during cyclic compression (30% strain) at frequencies from 0.3 Hz to 0.1 Hz.

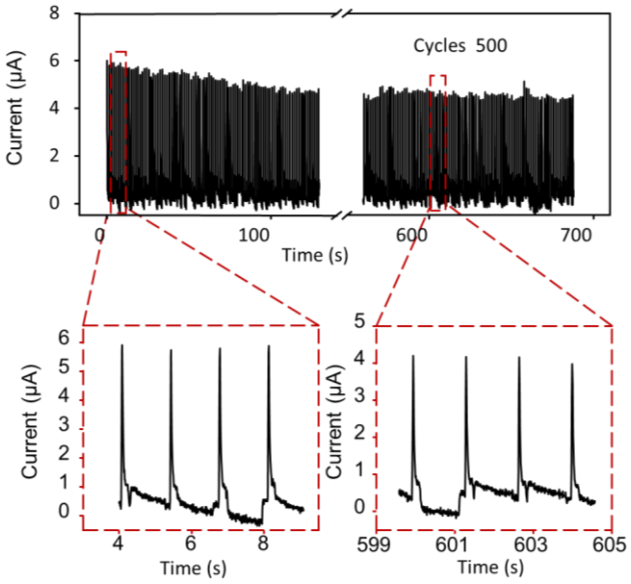

Supplementary Figure 27. Current response of the hydrogel e-skin over 500 compression cycles at 20% strain, showing less than 20% attenuation in output.

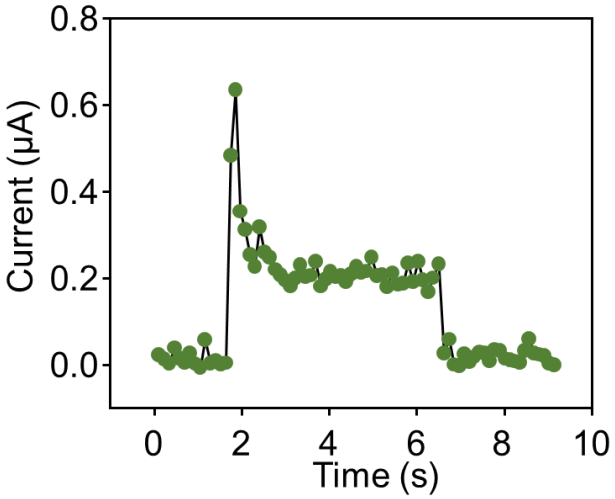

Supplementary Figure 28. Current response of the AMSG under a pressure of 60 Pa, generated by applying a 2.5 g weight to a 2 × 2 cm sensor.

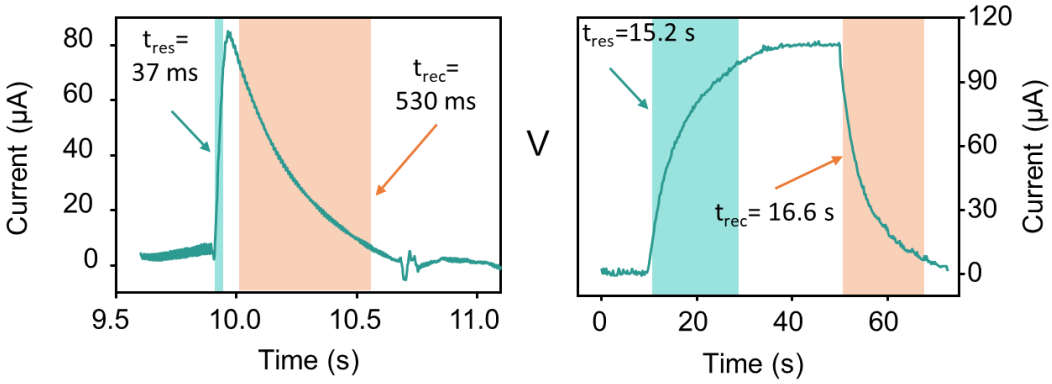

Supplementary Figure 29. Current responses and recovery times upon pressure (left) and temperature (right) stimuli, respectively.

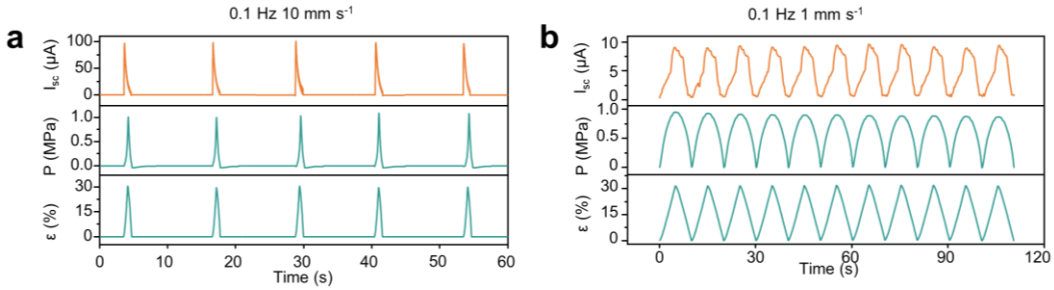

Supplementary Figure 30. Strain, stress, and current responses of the hydrogel e-skin at compression rates of 10 mm s^{-1} (left) and 1 mm s^{-1} (right) at a frequency of 0.1 Hz.

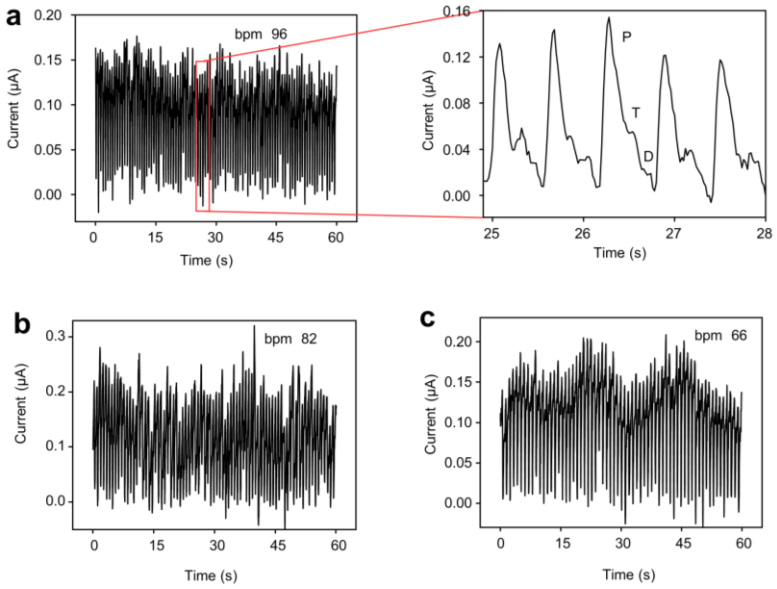

Supplementary Figure 31. Pulse waveforms measured under different physiological states, including (a) fever (with magnified pulse waveforms), (b) walking, and (c) sleep. The flexible woven wristband provides reliable back pressure for good contact between the sensor and the radial arteries.

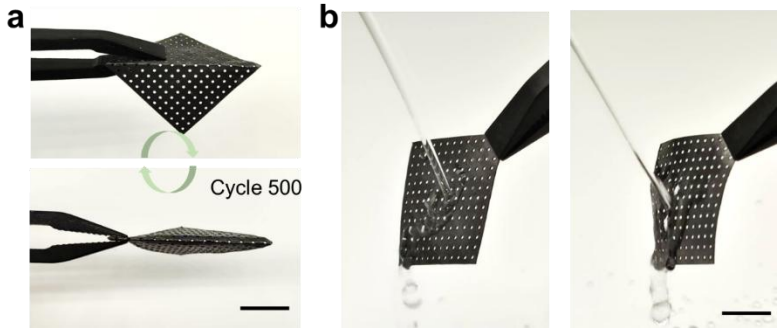

Supplementary Figure 32. Mechanical robustness of the porous electrode. (a) Electrodes remain in good working condition after 500 repeated folding cycles. (b) Electrodes remain intact under the impact of a high-pressure water jet.

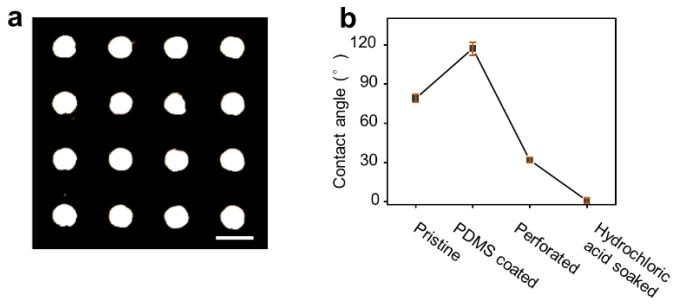

Supplementary Figure 33. (a) Microscopic image of the open electrode (scale bar: 1 mm). (b) Contact angle measurements of the electrode surface in different conditions.

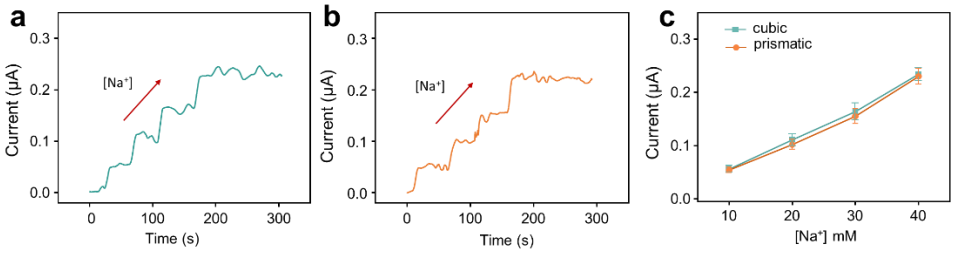

Supplementary Figure 34. Diffusion current comparison Between Prismatic (a) and Cubic (b) Structures. c Diffusion current against Na^+ concentration in prismatic and cubic structures. Hydrogel temperature maintained at 30 °C.

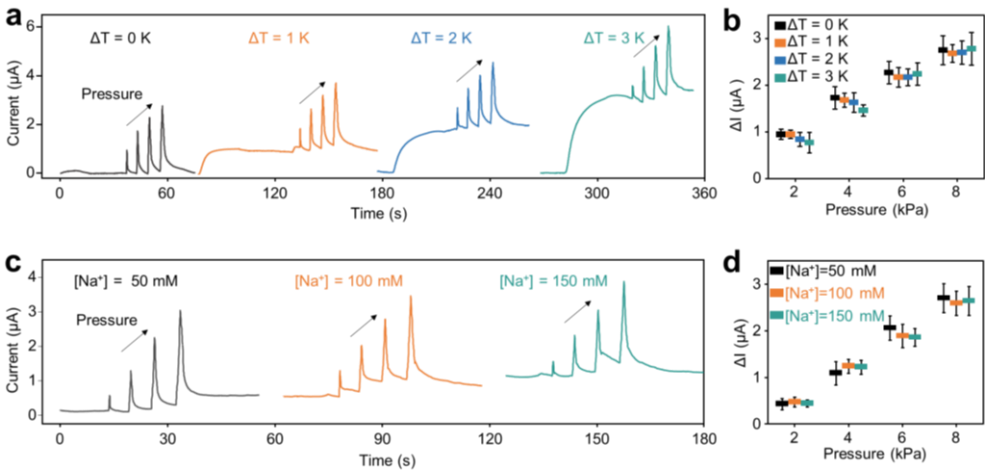

Supplementary Figure 35. (a) Piezoionic current at different temperature levels, where the cold end temperature is set to 30 °C, while the hot end temperatures are set to 30, 31, 32, and 33 °C, respectively. The applied pressures are 2, 4, 6, and 8 kPa, respectively. (b) Relationship between pressure and current variation (ΔI) at different temperature levels (ΔT). (c) Piezoionic current under different Na^+ concentrations, with applied pressures of 2, 4, 6, and 8 kPa, respectively. (d) Relationship between pressure and current variation (ΔI) under different Na^+ concentrations.

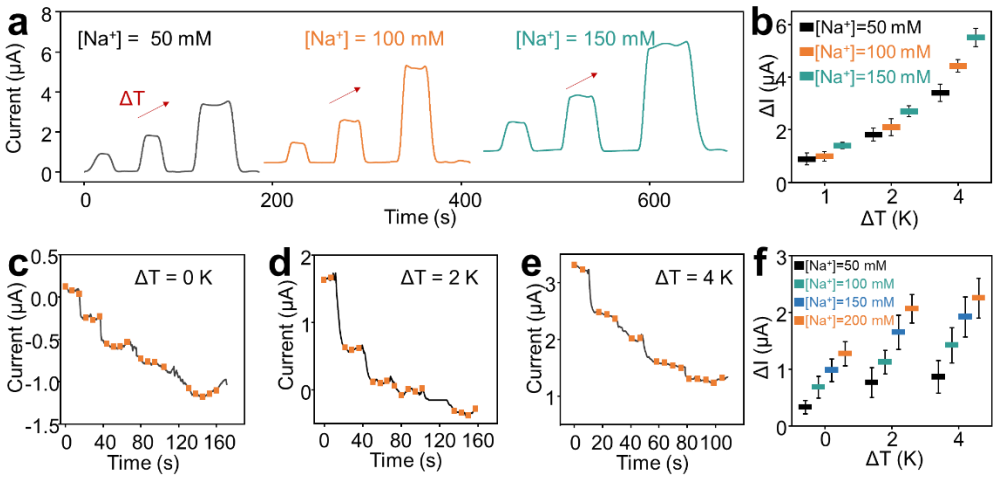

Supplementary Figure 36. (a) Thermoelectric current induced by different temperature differences at various Na^+ concentrations, with the hot junction temperature fixed at 30 °C. The cold junction temperatures were set to 29, 28, and 26 °C, respectively. (b) Thermoelectric response under different Na^+ concentrations. Time-dependent diffusion current curves during stepwise absorption of 50μL Na^+ solutions at different temperature differentials: (c) 0 K, (d) 2 K, (e) 4 K. The cold junction temperature was fixed at 30 °C. The hot junction temperature was set to 30, 32, and 34 °C, respectively. (f) Effect of Na^+ concentration on diffusion current variation (ΔI) under different temperature differences (ΔT).

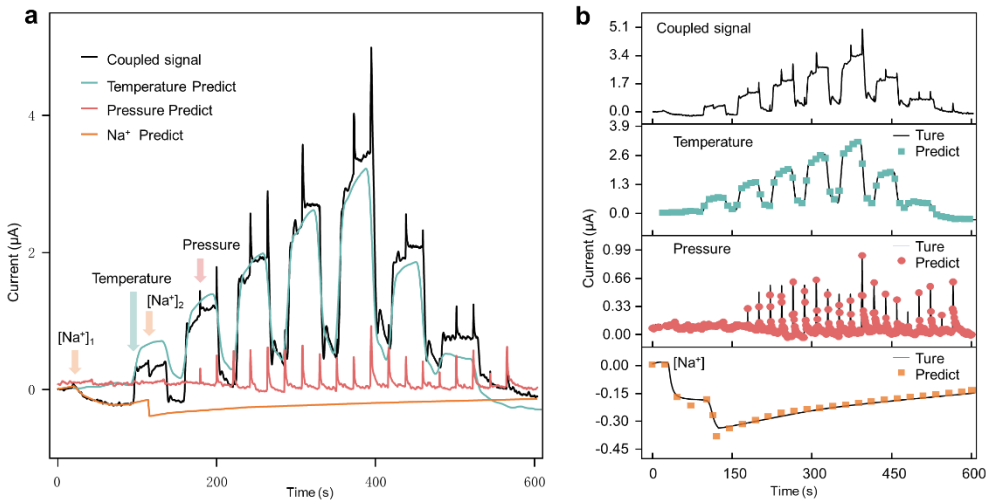

Supplementary Figure 37. (a) Coaxial plots of coupled signals and prediction curves for small variations in electrolyte, temperature, and pressure. Temperature was fixed at 30°C at the cold end, while the hot end varied from 30°C to 35°C. Pressure ranged from 0 to 3 N, and Na^+ concentration varied from 0 to 100 mM in two permeation steps. (b) Comparison of coupled signals and LSTM prediction results for electrolyte, temperature, and pressure on the same x-axis.

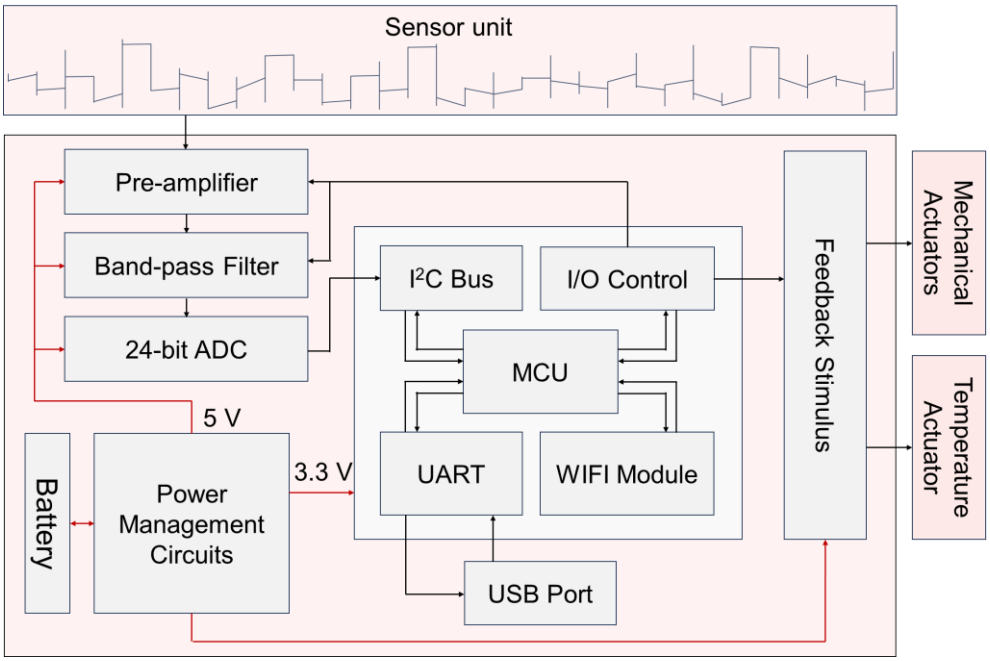

Supplementary Figure 38. Architecture of the multimodal sensing and feedback system, including signal processing, transmission, and power management.

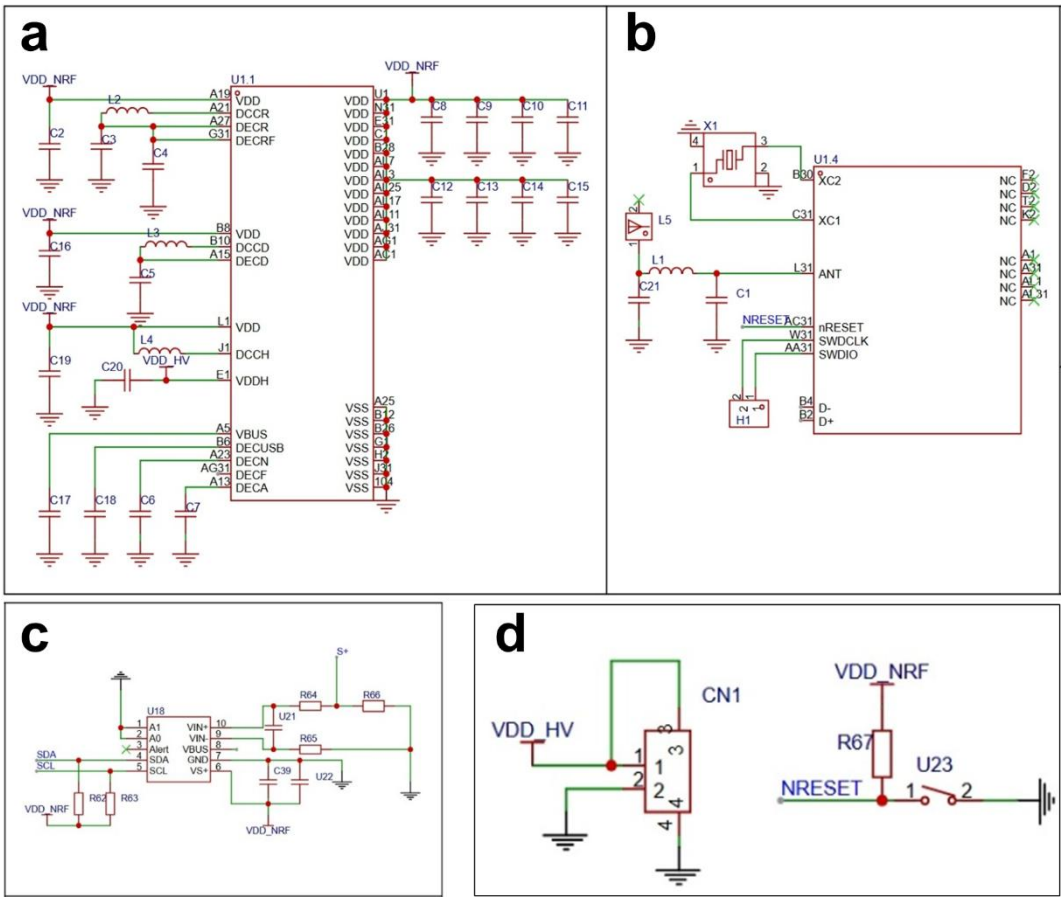

Supplementary Figure 39. Circuit Design of Wireless Current Acquisition Module. (a) Control and Data Processing Module. (b) Wireless Transmission Module. (c) Data Acquisition Module. (d) Power Supply and Reset Module.

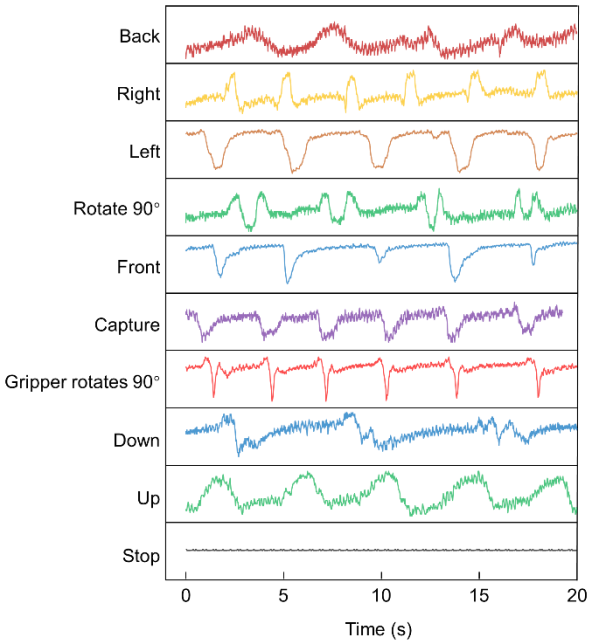

Supplementary Figure 40. Current responses of the AMSG during 10 gesture movements.

Supplementary Table 1. Comparison of flexible sensors

Refs	Self-powered	Multimodal sensing	Single-unit	Wearability	Response time
This work	√	√	√	Strain: 830% Modulus: 300 kPa	37 ms
[1] *Adv. Mater.* 34, 2205249 (2022)	×	√	√	Rigid	100 ms
[2] *Adv. Funct. Mater.* 34, 2314419 (2024)	√	×	√	Strain:530%	230 ms
[3] *Nat. Commun.* 16, 5689 (2025)	×	√	×	Rigid	N/A
[4] *Nat. Commun.* 16, 591 (2025).	×	×	×	Strain: 50% Modulus: 17 MPa	12 ms

Supplementary Table 2. Comparison of mechanical properties of IS with those of reported PVA gels.

Refs	Content (wt %)	Stretchability (100%)	Toughness (MJ m^{-3})	Stiffness (MPa)	Fracture energy (KJ m^{-2})	Method
This work	15% PVA	830	7.72	0.32	50.4	Freeze-thaw +Double Solvent-exchange
M. Hua, S. Wu, Y. Ma, Y. Zhao, Z. Chen, I. Frenkel, J. Strzalka, H. Zhou, X. Zhu, X. He, Nature 2021, 590, 594.	5%-20% PVA	2900	210	N/A	170	Directional freezing + Salting out
Y. Wu, Y. Zhang, H. Wu, J. Wen, S. Zhang, W. Xing, H. Zhang, H. Xue, J. Gao, Y. Mai, Adv. Mater. 2023, 35, 2210624.	15% PVA	1879	82.28	2.67	25.3	Solvent-exchange+ Wet-annealing
N. Li, Z. Wang, X. Yang, Z. Zhang, W. Zhang, S. Sang, H. Zhang, Adv. Funct. Mater. 2024, 34, 2314419.	15%PVA	535	~0.48	~0.027	N/A	3 freeze-thaw cycles
L. Liu, D. Zhang, P. Bai, Y. Mao, Q. Li, J. Guo, Y. Fang, R. Ma, Adv. Mater. 2023, 35, 2300696.	15%PVA	1300	163.4	~1.94	N/A	Stretch induction+ Freeze-thaw
C. Bai, X. Li, X. Cu, X. Yang, X. Zhang, K. Yang, T. Wang, H. Zhang, Nano Energy 2022, 100, 107449.	11%PVA+ 1% gelatin	240	0.72	~0.25	N/A	3 freeze-thaw cycles

C. Adu, S. Rahatekar, J. Filby, D. Ayre, M. Jolly, Mater. Lett. 2019, 253, 242-245.	2%PVA+2 %CNF+0.5 % borax	40	N/A	N/A	N/A	Directional freezing+ Freeze dry
X. Li, J. Li, T. Wang, S. Khan, Z. Yuan, Y. Yin, H. Zhang, ACS Appl. Mater. Interfaces 2022, 14, 48743−48751.	11%PVA+ 1% gelatin	320	0.57	0.13	N/A	3 freeze-thaw cycles

Supplementary Table 3. Comparison of mechanical and strain sensing performance, including S_e, stretchability, pressure response time, and temperature response time of the hydrogel e-skin with those of reported quasi-solid stretchable thermogalvanic thermocells.

Refs	$\|S_e\|$(mV K-1)	Strain	Pressure response time (s)	Temperature response time (s)
This work	1.61	830 %	0.037	15.2
J. Shen, C. Yang, Y. Ma, M. Cao, Z. Gao, S. Wang, J. Li, S. Liu, Z. Chen, S. Li, EcoMat. 2024, 6, e12428.	1.4	N/A	N/A	~180
P. Peng, Z. Li, D. Xie, K. Zhu, C. Du, L. Liang, Z. Liu, G. Chen, J. Mater. Chem. A, 2023, 11, 6986.	1.02-1.29	300	N/A	~300
N. Li, Z. Wang, X. Yang, Z. Zhang, W. Zhang, S. Sang, H. Zhang, Adv. Funct. Mater. 2024, 34, 2314419.	1.82	534.5	0.23	~35
L. Liu, D. Zhang, P. Bai, Y. Mao, Q. Li, J. Guo, Y. Fang, R. Ma, Adv. Mater. 2023, 35, 2300696.	6.5	1300	N/A	~210
C. Bai, X. Li, X. Cu, X. Yang, X. Zhang, K. Yang, T. Wang, H. Zhang, Nano Energy 2022, 100, 107449.	1.48	240	N/A	N/A
C. Han, X. Qian, Q. Li, B. Deng, Y Zhu, Z. Han, W. Zhang, W. Wang, S. Feng, G. Chen, W. Liu, Science 2020, 368, 1091-1098.	17.0	200	N/A	2400

X. Li, J. Li, T. Wang, S. Khan, Z. Yuan, Y. Yin, H. Zhang, ACS Appl. Mater. Interfaces 2022, 14, 48743−48751.	1.29	320	N/A	170

Supplementary Table 4. Comparison of gauge factor (GF), sensing mechanism, self-powered capability, and contact/non-contact sensing capability between this work and the reported literature.

Refs	GF	Sensing mechanism	Self-powered	Contact/ Non-contact Sensing
This work	18.70-175.30	Temperature+ strain+ electrolyte	Yes	Non-contact
Y. Ni, X. Zang, Y. Yang, Z. Gong, H. Li, J. Chen, C. Wu, J. Huang, Y. Lai, Adv. Funct. Mater. 2024, 2402853.	45.90-103.40	Humidity	No	Non-contact
T. Zhang, Y. Ding, C. Hu, M. Zhang, W. Zhu, C. Bowen, Y. Han, Y. Yang, Adv. Mater. 2022, 2203786.	N/A	Strain	Yes	Contact
N. Li, Z. Wang, X. Yang, Z. Zhang, W. Zhang, S. Sang, H. Zhang, Adv. Funct. Mater. 2024, 34, 2314419.	1.35-4.92	Strain	Yes	Contact
X. Li, J. Li, T. Wang, S. Khan, Z. Yuan, Y. Yin, H. Zhang, ACS Appl. Mater. Interfaces 2022, 14, 48743−48751.	N/A	Temperature	Yes	Contact
J. Zhang, S. Shen, R. Lin, J. Huang, C. Pu, P. Chen, Q. Duan, X. You, C. Xu, B. Yan, X. Gao, Z. Shen, L. Cai, X. Qiu, H. Hou, Adv. Mater. 2023, 35, 2209497.	0.90	Strain	No	Contact
L. Zhao, H. Xu, L. Liu, Y. Zheng, W. Han, L. Wang, Adv. Sci. 2023, 10, 2303922.	0.98	Strain	No	Contact

M. Pi, S. Qin, S. Wen, Z. Wang, X. Wang, M. Li, H. Lu, Q. Meng, W. Cui, R. Ran, Adv. Funct. Mater. 2023, 33, 2210188.	1.24-1.92	Strain	No	Contact

Supplementary Table 5. The initial configuration setup for simulation system.

	Number of H_2O	Number of Fe^{2+}	Number of Fe^{3+}	Number of Cl^-	Number of PVA
System	2800	5	5	25	5

Supplementary Table 6. Matrix property parameters used in the COMSOL numerical model for piezoionic simulation.

Parameter name	Value
Polymer matrix modulus	10^5 Pa
Polymer matrix permeability	$2 \cdot 10^{-13}$ m^2
Polymer matrix Poisson's ratio	0.499
Polymer matrix density	1.1 g cm^{-3}
Fluid density	1 g cm^{-3}
Fluid viscosity	$1.3 \cdot 10^{-3}$ Pa·s

References

1. Martínez, L., Andrade, R., Birgin, E. G. & Martínez, J. M. P ACKMOL : A package for building initial configurations for molecular dynamics simulations. *J Comput Chem* **30**, 2157–2164 (2009).

2. Sambasivarao, S. V. & Acevedo, O. Development of OPLS-AA Force Field Parameters for 68 Unique Ionic Liquids. *J. Chem. Theory Comput.* **5**, 1038–1050 (2009).

3. Dong, X. *et al.* Strong and Tough Conductive Organo-Hydrogels via Freeze-Casting Assisted Solution Substitution. *Adv. Funct. Mater.* **32**, 2203610 (2022).

4. Hua, M. *et al.* Strong tough hydrogels via the synergy of freeze-casting and salting out. *Nature* **590**, 594–599 (2021).

5. Everaers, R. & Kremer, K. A fast grid search algorithm for molecular dynamics simulations with short-range interactions. *Comput. Phys. Commun.* **81**, 19–55 (1994).